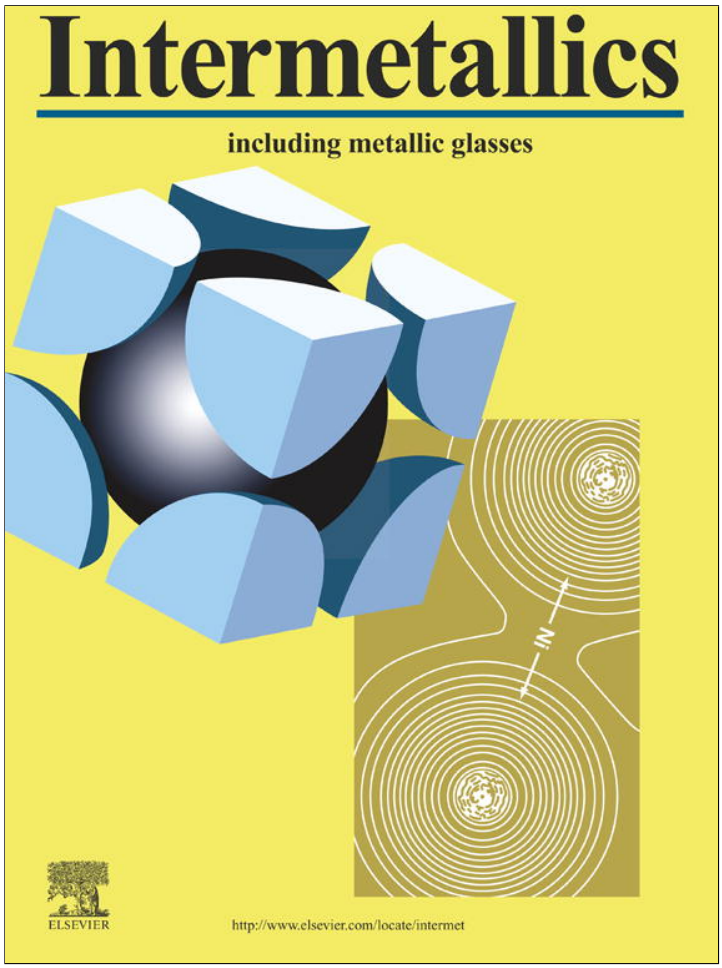

Intermetallics 39 (2013) 25–33

Contents lists available at SciVerse ScienceDirect

Intermetallics

journal homepage: www.elsevier.com/locate/intermet

An in-situ high-energy X-ray diffraction study on the hot-deformation behavior of a β-phase containing TiAl alloy

T. Schmoelzer [a,*], K.-D. Liss [b], C. Kirchlechner [c], S. Mayer [a], A. Stark [d], M. Peel [e], H. Clemens [a]

[a] Department of Physical Metallurgy and Materials Testing, Montanuniversität Leoben, Franz-Josef Strasse 18, 8700 Leoben, Austria
[b] Australian Nuclear Science and Technology Organisation, Lucas Heights, New South Wales 2232, Australia
[c] Department Material Physics, Montanuniversität Leoben, 8700 Leoben, Austria
[d] Institute of Materials Research, Helmholtz-Zentrum Geesthacht, 21502 Geesthacht, Germany
[e] Department of Mechanical Engineering, University of Bristol, Bristol, UK

ARTICLE INFO

Article history:
Received 15 February 2012
Received in revised form
24 September 2012
Accepted 12 February 2013
Available online

Keywords:
A. Titanium aluminides, based on TiAl
C. Thermomechanical treatment
F. Diffraction
G. Aero-engine components

ABSTRACT

In engineering materials, microstructural evolution during hot-working critically determines the properties of the finished part. Intermetallic TiAl alloys are no exception and numerous attempts have been made to improve their performance by subjecting them to harmonized hot-working steps. In the current work a novel in-situ diffraction technique along with conventional microscopic methods were employed to characterize the behavior of the individual phases at two different deformation temperatures. A so-called TNM™ alloy with a nominal composition of Ti-43.5 Al-4 Nb-1 Mo-0.1 B (in at%), which exhibits an adjustable fraction of disordered β-phase at elevated temperatures, was deformed isothermally at 1220 °C and 1300 °C. At 1220 °C three phases (α,β,γ) are present in thermodynamic equilibrium which reduces to two (α,β) at 1300 °C. It was possible to observe in-situ the individual behavior of the involved phases during deformation and the phenomena which accommodate the defects generated by hot-working. Results of post-mortem microscopic investigations were used to confirm the findings. The results of the in-situ experiments give unique insights into the hot-deformation behavior of multi-phase TiAl alloys, which can be used for specific process optimization and for further alloy development.

1. Introduction

Intermetallic γ-TiAl alloys exhibit high strength at elevated temperatures while having low density [1–5]. These properties make them an attractive material for the application in turbine blades of aero-engines as well as in turbocharger turbine wheels for reciprocating engines [6–9]. Due to the continuous strive of manufacturers to improve engine efficiencies, the demands on the performance of components are ever increasing. A transition in the production route, from casting toward implementation of a hot-working step, combined with subsequent heat-treatments is expected to enable a more thorough control of the microstructure and thus improve the mechanical properties of the finished part [10–12].

Alloys of the so-called TNM™ family can be forged using an isothermal or a near-conventional process [7,13,14]. This type of alloy is particularly well suited for forging and rolling due to the presence of the ductile, disordered, body-centered cubic (bcc) β-phase at hot-deformation temperatures [10,13,15]. While it is well established that the β-phase promotes the hot-deformation behavior [16–18], it is not clear which microstructural mechanisms act during forging. A number of papers have been published concerning the hot-deformation of γ-TiAl alloys, mostly reporting on compression experiments performed at different temperatures and strain rates where the specimens were subjected to subsequent microstructural investigations [19–25]. Such post-mortem investigations are complicated by the fact that multiple phase transformations and ordering reactions may occur upon cooling to room-temperature. Information on phase equilibria and transformation temperatures in the Ti–Al system can be found elsewhere [26]. Recent studies on the pseudo-binary phase diagram of TNM™ alloys are also available [27–29]. A second method derives microstructural information from the shape of the flow-curve which is determined by the deformation response of each individual phase and their interactions [20,22–24]. In practice, the flow-curve predominantly reflects the behavior of the majority phase. Additionally, it is notable that most experiments on TiAl alloys have been conducted within the $(\alpha_2+\gamma)$, $(\alpha+\gamma)$ or $(\alpha+\beta_o+\gamma)$

* Corresponding author. Tel.: +43 3842 4024201; fax: +43 3842 4024202.
E-mail addresses: tom.schmoelzer@gmail.com, thomas.schmoelzer@schmoelzer.net (T. Schmoelzer).

0966-9795/$ – see front matter © 2013 Elsevier Ltd. All rights reserved.
http://dx.doi.org/10.1016/j.intermet.2013.02.016

phase field regions. Consequently, little information concerning deformation at very high temperatures, i.e. in the $(\alpha + \beta)$ phase field region is available.

In this study, an attempt was made to observe the behavior of a β-containing TiAl alloy in-situ during hot-deformation. To this end, a high-energy X-ray diffraction (HEXRD) method developed by Liss et al. was utilized [30–32]. The findings obtained by the in-situ method were confirmed by the results of post-mortem microstructural investigations. Performing in-situ experiments at two different temperatures – in the $(\alpha + \beta)$ and the $(\alpha + \beta + \gamma)$ phase field regions – allows comparison of the deformation behavior dependent on the phases present. The obtained results ultimately contributed to determining suitable process parameters for industrial forming operations [12,13].

2. Materials and methods

The alloy investigated had a nominal chemical composition of Ti-43.5 Al-4 Nb-1 Mo-0.1B (in at%) and was supplied by GfE Metalle und Materialien GmbH, Nuremberg, Germany. Ingots with a diameter of 55 mm were produced by means of centrifugal casting. To close residual porosity, the ingot was subsequently hot-isostatically pressed (HIP) at a temperature of 1200 °C and a pressure of 200 MPa for 4 h. The three main phases are the α_2-Ti_3Al ($D0_{19}$ structure), the β_o-Ti phase (B2 structure) as well as their disordered polymorphs (α: A3 structure, β: A2) and the γ-TiAl phase ($L1_0$). The β/β_o-phase fraction has a minimum at 1285 °C which is also the transition temperature between the $(\alpha + \beta)$ and $(\alpha + \beta + \gamma)$ phase field region. A pseudo-binary section of the phase diagram calculated with a commercial TiAl data base [33] is presented in Fig. 1a. Alloy composition and deformation temperatures used in the current study are indicated. The course of phase fractions over temperature shown in Fig. 1b was acquired during a previous study [28]. For further details, especially on the difference between calculated and experimentally established phase diagrams, the reader is referred to Refs. [27–29]. At 1300 °C, i.e. in the $(\alpha + \beta)$ phase field region, the volume fractions of α and β are approximately 93 vol% and 7 vol% whereas at 1220 °C, volume fractions of α, β, and γ were determined to 46 vol%, 13 vol%, and 41 vol% respectively. In Fig. 1b, the $\beta_o \leftrightarrow \beta$ and $\alpha_2 \leftrightarrow \alpha$ order/disorder temperatures obtained from neutron diffraction experiments are indicated [34]. As the phenomena occurring during deformation are discussed, it should be born in mind that the experiments were conducted at very high homologous temperatures. A deformation temperature of 1300 °C corresponds to approximately $0.87 \times T_m$ whereas 1220 °C are equivalent to $0.82 \times T_m$.

The experimental setup for investigating dynamic microstructural processes with high-energy X-rays [35] is based on a conventional powder diffraction experiment at a synchrotron source. In the illuminated specimen volume, a limited number of grains should be contained to be able to distinguish single diffraction spots from individual crystallites lying on the Debye–Scherrer rings. Yet a sufficiently high number of grains have to be observed to allow drawing conclusions about the prevailing microstructure. A suitable condition was achieved by using a monochromatic beam with a mean energy of 86.94 keV and a cross-section of 0.1×0.1 mm^2 as well as cylindrical specimens with a diameter of 4 mm and a length of 8 mm. Diffraction patterns were recorded at a frame rate of about 2 Hz by a Pixium 4700 flat panel detector [36] (Thales Group, Neuilly-sur-Seine, France) which was placed at a distance of 1233.8 mm from the specimen position. The sample-detector distance was determined by means of triangulation and the mean energy of the beam calibrated by employing a CeO_2 standard.

An electro-thermomechanical tester (ETMT) (Instron, Norwood, MA, USA) was utilized for heating and deforming the samples. With this device, heating was achieved resistively with a maximum current of 450 A at 8 V while mechanical loads of up to 3 kN can be imposed on the specimen. The temperature was measured with a type S thermocouple formed to a melt bead which was spot-welded directly onto the specimen surface. Inserting Ta and graphite foil between the specimen and the anvils provided a diffusion barrier and decreased friction forces at the interface. Since the ETMT has a moving and a stationary anvil, the motorized table that carried the ETMT was controlled in such a way that the beam illuminated the same specimen volume throughout the entire experiment.

The specimens were heated to the intended temperatures (1220 °C and 1300 °C) at a rate of 10 °C/s and held at this temperature for 30 s. Then, compression started with a constant anvil speed of 0.021 mm/s which translates to a mean strain rate of 3.7×10^{-3} s^{-1}. During the experiment performed at 1300 °C, deformation was discontinued for 20 s to investigate the corresponding materials response. Although the experiment was set up for isothermal deformation the temperature started to decrease at high strains. This was caused by the increase in specimen diameter during compression leading to a decrease in electrical resistance and, correspondingly, the heating power. After a total strain of $\varphi \sim -0.9$, the experiments were terminated. To validate the stress–strain data obtained with the ETMT, hot-compression experiments

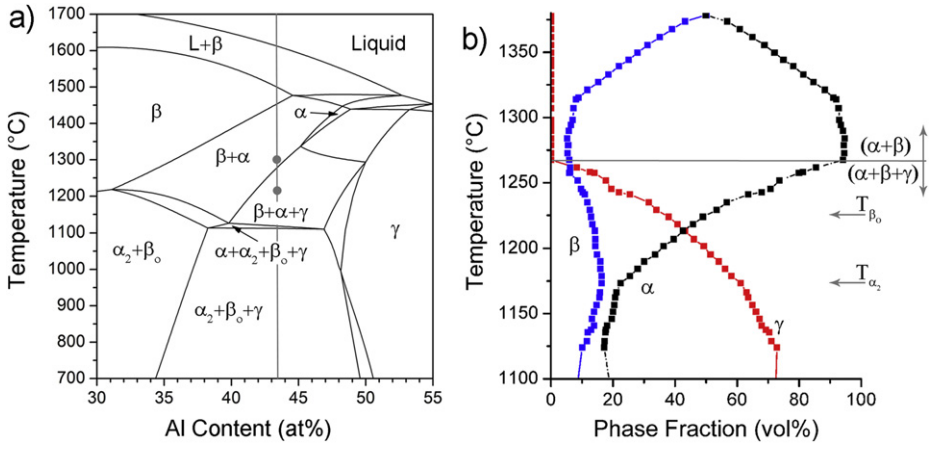

Fig. 1. (a) Calculated binary section of the quaternary phase diagram [27] and (b) experimentally determined course of phase fractions over temperature of the investigated alloy [28]. In (a), the alloy composition is indicated by a vertical line, the two deformation temperatures are marked by filled circles. Order/disorder transition temperatures of α_2/α and β_o/β are indicated by $T_{\alpha 2}$ and $T_{\beta o}$, respectively in (b) [34].

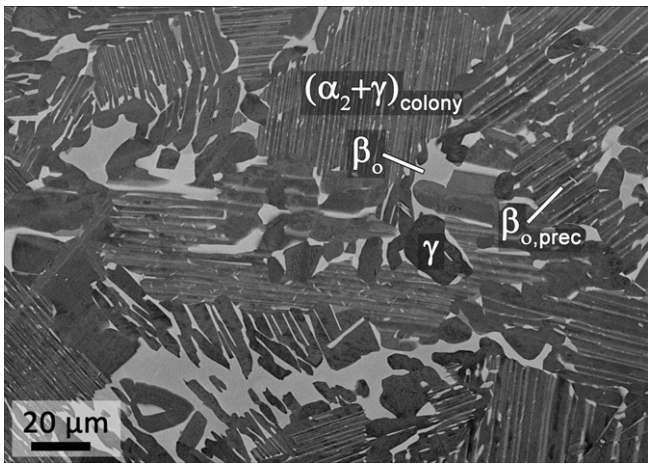

Fig. 2. Microstructure of the cast and HIP starting material. Three phases are present of which β_o images brightest, α_2 appears in an intermediate shade of grey and γ is the darkest phase. The image was obtained by means of SEM in BSE contrast.

were conducted on a Gleeble thermomechanical simulator at a constant strain rate of 5×10^{-3} s^{-1} and temperatures of 1200 °C and 1300 °C [37].

As dynamic processes are occurring in the microstructure of the specimen, both during heating and deformation, the morphology of the reflection spots on the Debye–Scherrer rings changes. Broadening of a spot is caused by the introduction of defects into the lattice. Sub-grain formation may be identified by the dissociation of one diffraction spot into a distribution cone characterized by its mosaic spread, or, if resolved, into a set of individual peaks within a narrow angular range [38]. A crystallite of small size is represented by a sphere of finite radius rather than a point in reciprocal space and, hence, produces also a broader diffraction spot [39]. Additionally, if the diffraction patterns are recorded continuously, grain rotation can be detected during plastic deformation [40,41]. It has, however, to be born in mind that a grain which satisfies the Bragg-condition only continues to do so if its rotation axis is parallel to the incident beam. Texture evolution during hot-working becomes evident in the intensity distribution over the azimuthal angle and the different Debye–Scherrer rings [41]. In a kinematic approximation, the intensity of the individual diffraction spots is proportional to the volume of the corresponding crystallites [39]. More details on the employed diffraction method can be found in Refs. [30–32,42,43]. To illustrate the development of reflections with time, the intensity on one Debye–Scherrer ring is plotted in greyscale as a function of azimuthal angle and time. In these azimuthal angle time plots (called AT-plots henceforth) a stationary reflection spot produces a continuous line. If the line is tilted, the spot (and hence, the grain) rotates about the beam axis. Such lines are called timelines in the following. More details on the generation and interpretation of an AT-plot can be found in Refs. [31,32]. Changes in phase fraction during the experiment were determined by calculating the area under all easily distinguishable reflections of the considered phase and relating the value to the total area under all reflections of the pattern.

After completion of the experiments, microstructural investigations were performed on the deformed specimens. Micrographs were obtained on a Zeiss EVO 50 scanning electron microscope (SEM) at an acceleration voltage of 20 kV in back scattered electron (BSE) imaging mode. Electron backscatter diffraction (EBSD) images were obtained on an LEO field emission gun SEM (Zeiss 1225) equipped with an EDAX EBSD system. An acceleration voltage of 30 kV and a 120 µm aperture were used for image acquisition.

3. Results

After casting and HIP, the material exhibits a microstructure as shown in Fig. 2. In this condition, colonies consisting of coarse α_2 and γ lamellae as well as globular γ-grains are present. The lamellar colonies have a broad size distribution with the largest ones reaching lengths of up to 200 µm, whereas the maximum diameter of the globular γ-grains is about 20 µm. A substantial amount of β_o-phase is observed which encompasses the lamellar colonies. Additionally, small β_o precipitates can be found within the α_2-laths of the lamellar colonies. It should be noted that the relatively fine-grained cast microstructure shown in Fig. 2 is achieved by the addition of boron. A good chemical homogeneity is attained by solidification via the β-phase [10].

Microstructural images obtained from the specimens deformed during the in-situ HEXRD experiments at 1300 °C and 1220 °C are depicted in Fig. 3. Due to the high cooling rate, the two-phase ($\alpha + \beta$) microstructure present at a deformation temperature of 1300 °C was preserved in 3 a. Upon cooling, only the $\alpha \rightarrow \alpha_2$ and $\beta \rightarrow \beta_o$ ordering reactions took place. The β_o-grains have attained a form that is more elongated perpendicular to the compression direction than the α-grains. Additionally, the complex shapes of the β_o-grains should be noted. Fig. 3b shows a microstructural image of the specimen deformed at 1220 °C in the ($\alpha + \beta + \gamma$) phase field. Consequently all three phases are observed in the micrograph. The γ-phase is present in the form of globular grains and coarse

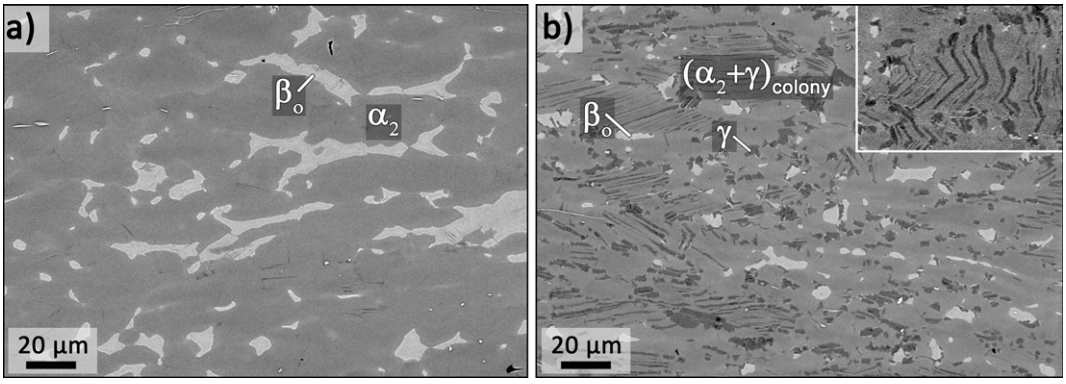

Fig. 3. Microstructures after deformation at 1300 °C (a) and 1220 °C (b). In (a) only α_2 and β_o-phase are present while in (b) also γ-phase is evident. Labels in the micrographs indicate the phases present during hot-deformation. The inset in (b) shows lamellae that buckled during compression. In both images the compression direction is vertical and the scale of the inset is identical to the main image (b).

lamellae within colonies, some of which have buckled during deformation. It is worth mentioning that no γ-lamellae oriented parallel to the compression direction were observed. Lamellae that buckled during deformation appear to have been the ones that were initially parallel to the loading axis (Fig. 3b inset). Compared to the starting microstructure (Fig. 2), grain refinement is more pronounced in the specimen deformed at 1220 °C (Fig. 3b) than in the one deformed at 1300 °C (Fig. 3a).

AT-plots of the deformation experiments performed at 1300 °C and 1220 °C as well as the parameters temperature, true stress, and true strain are presented in Fig. 4a–f. For two representative reflections, α 022 (Fig. 4a) and β 002 (Fig. 4b), the development of diffraction patterns over time is given only for azimuthal angles between 0° and 180° to avoid the use of overly large images.

Fig. 4c and f shows the development of temperature, true stress and true strain as a function of time. Both experiments were performed isothermally except for the aforementioned cross-section related temperature decrease toward the end of the test, which led to an increase in flow-stress [20,24]. Deformation was intentionally discontinued for 20 s during the experiment performed at 1300 °C to be able to observe static annealing phenomena.

During continuous heating to 1300 °C, at about 1280 °C, a sudden change in the intensity of α reflections occurs (Fig. 4a) signifying the dissolution of the γ-phase. Some of the β spots intensify and new ones are appearing (Fig. 4b). While holding at 1300 °C, the α-phase reflections are static, whereas the β spots show some degree of fluctuation. As deformation starts, α-phase timelines tilt, some bifurcate and all of them broaden. In the AT-plots of the β-phase, dot-clouds are formed almost instantaneously. After 217 s, deformation was discontinued and the static behavior of the material can be observed.

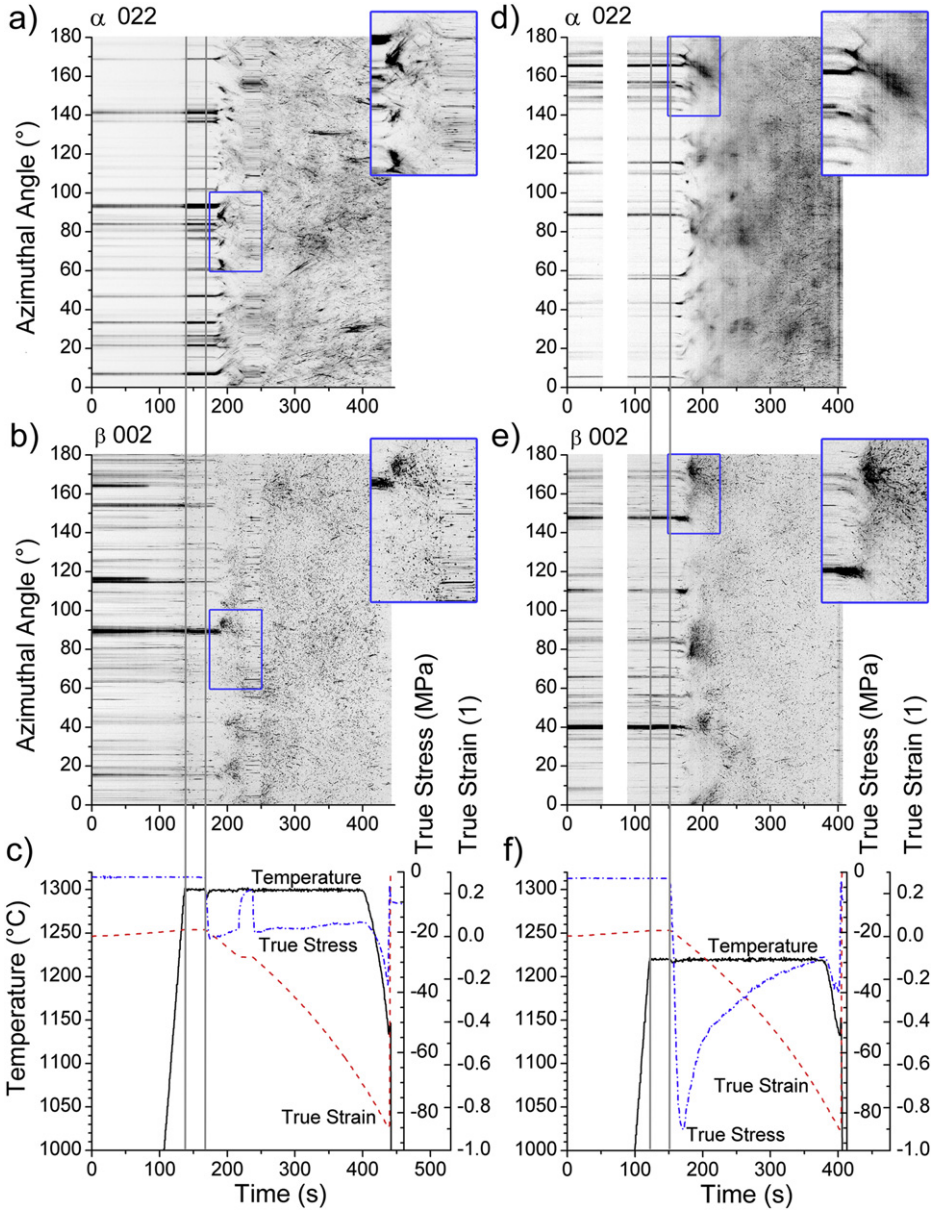

Fig. 4. AT-plots of specimens deformed at 1300 °C (left column) and at 1220 °C (right column). Both, α 022 (a,d) and β 002 (b,e) reflections are imaged as well as temperature, true stress and true strain (c,f) throughout the hot-compression experiment. During heating, the temperature increases linearly from RT to deformation temperature. Temperature values below 1000 °C are omitted to improve readability. The vertical lines indicate reaching of the deformation temperature and the onset of loading while the insets provide a magnified view of pattern development at the beginning of deformation.

For both phases the number of timelines observed while deformation was stopped is greater than that before the onset of deformation. This indicates that grain refinement has occurred. Once more, the α-phase grains produce timelines in which only a few intensity fluctuations are present. The β-phase, on the other hand, exhibits strongly fluctuating intensity. As deformation continues at 1300 °C, the α-phase timelines tilt again, whereas those of the β-phase disintegrate into dots. Upon further deformation only dots are observed in the AT-plot of the β-phase (Fig. 4b). The plot of the α-phase, on the other hand, reveals a few timelines of high intensity that are inclined with respect to the time axis (Fig. 4a). Generally, timelines of the α-phase are longer than those of the β-phase.

The AT-plots of α and β-phase of the experiment performed at 1220 °C are shown in Fig. 4d and e. No images were acquired between 54 s and 89 s due to the fact that the detector routine was interrupted and had to be restarted. Since no fluctuations occur in the α or β-phase after the period during which no images were recorded, it can be assumed that no important microstructural developments were missed during heating. Again, during the holding time only the β reflections fluctuate in intensity (Fig. 4d and e). As deformation commences, the α-phase timelines instantly broaden and are increasingly blurred as deformation increases. Starting at 270 s, comparably sharp reflection dots are appearing in the AT-plot of the α-phase. The AT-plot of the β-phase reveals the splitting of timelines into dot-clouds when deformation starts and only a few short, comparably sharp timelines are observed until the final deformation is attained (Fig. 4e).

In the investigated alloy, also γ-phase is present at 1220 and the AT-plot of its 020 reflection is presented in Fig. 5a. During heating, only gradual changes in intensity are observed. Similar to all other phases the majority of γ timelines broaden as deformation starts. Some, however, remain sharp for a long period of time (see inset in Fig. 5a). With increasing strain sharp dots appear which are of low intensity. Single timelines are increasingly difficult to see as deformation progresses.

As expected, large changes in phase fractions occurred in both experiments while the specimens were heated to the deformation temperature. For the dependence of phase fractions on temperature of the investigated alloy the reader is referred to Ref. [28]. From the development of phase fractions during the holding time it is concluded that conditions close to the thermodynamic equilibrium are attained after 30 s. No significant change in phase fractions was observed during compression of the specimens.

The load imposed on the specimen and the anvil position were recorded throughout the experiment. Together with the starting geometry of the specimens, these data allow calculating the true stress and true strain under the assumptions that the specimens retain a cylindrical shape and their volumes remain constant. Stress–strain curves that were attained in this fashion are featured in Fig. 6. After loading, the curve obtained at 1300 °C exhibits a fairly constant flow-stress of around −20 MPa. The discontinuity in the curve stems from the short period of time during which the deformation was paused. In contrast, the flow-stress at 1220 °C rises rapidly to −80 MPa just after just after deformation commences before it starts to decline gradually.

After deformation, the specimens used in the in-situ experiments were investigated with regard to their microstructure by means of EBSD. Kernel average misorientation maps of the specimen deformed at 1300 °C are presented in Fig. 7. In this mode, the misorientations between a center point and its next-nearest neighbors are evaluated. The average misorientation is then calculated and assigned to the center point. Details on this procedure can be found in Refs. [44,45]. A number of sub-grain boundaries are visible in the α_2-phase grains. Additionally, high degrees of misorientation are observed within some grains. In contrast to this, the β_o grains exhibit rather low defect densities.

In Fig. 8, kernel average misorientation maps of the specimen deformed at 1220 °C are shown. At this temperature three phases (α, β and γ) were present during deformation. Due to the precipitation of fine γ-lamellae during cooling (after deformation), the α_2-phase was not properly resolved in the EBSD image. The γ-phase is only imaged if present in the form of globular grains or coarse lamellae. In these areas, some low-angle grain boundaries (LAGB)

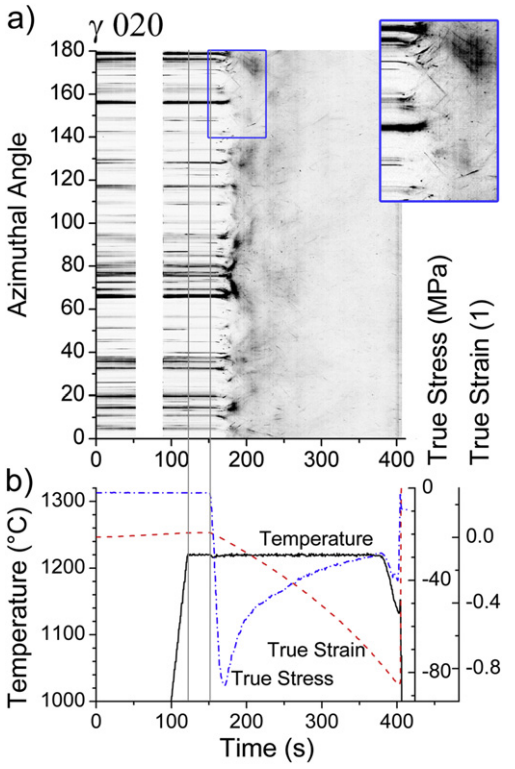

Fig. 5. (a) AT-plot of the γ 020 reflection of the specimen deformed at 1220 °C and (b) the corresponding deformation parameters. In the inset, a section of the AT-plot is magnified. Temperature values below 1000 °C are omitted to improve readability. Vertical lines indicate reaching of the deformation temperature and the onset of loading.

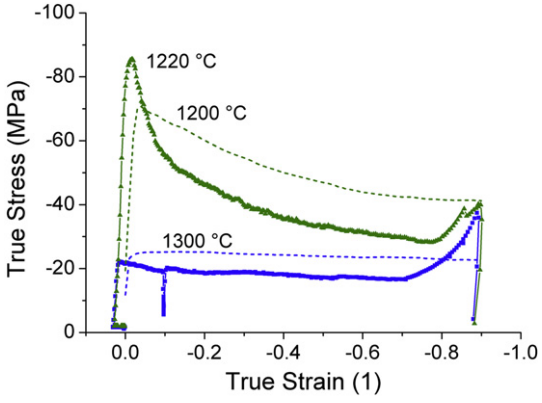

Fig. 6. Stress–strain curves of specimens deformed at 1300 °C (α + β phase field region) and 1220 °C (α + β + γ phase field region). The data were acquired during the in-situ experiment where the specimen was deformed at a mean strain rate of 3.7×10^{-3} 1/s. The dashed lines show the results of experiments conducted with a Gleeble thermomechanic simulator at temperatures of 1200 °C and 1300 °C at a strain rate of 5×10^{-3} s^{-1} [37].

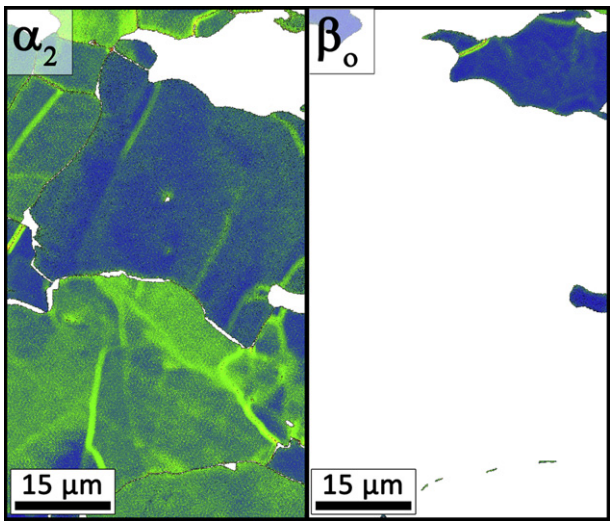

Fig. 7. Kernel average misorientation maps of α_2 and β_o-phase obtained by EBSD (light colors correspond to high misorientations). The images show the microstructure of the specimen after deformation at 1300 °C. Note that both phases were disordered at 1300 °C.

and orientation gradients within grains are observed. It is obvious from Fig. 8 that, apart from a few LAGB, only a low number of defects were stored in the β_o-phase. The misorientation plot of the γ-phase reveals the presence of sub-grain boundaries and of certain areas of high misorientation especially in coarse lamellae.

4. Discussion

The reason for implementing complex hot-deformation steps in the production route of TiAl parts is to improve the microstructure and therefore the mechanical properties of the product [1,2,4,7,46,47]. A comparison between the microstructures present before (Fig. 2) and after (Fig. 3) hot-deformation shows that the grains were elongated perpendicular to the compression direction during plastic deformation. After hot-compression at 1220 °C, many lamellar grains are oriented with the lamellae perpendicular to the load axis (Fig. 3b). This observation is explained by the fact that lamellar colonies exhibit a deformation behavior that is similar to a stack of cards. If the lamellae are perpendicular to the loading direction, the colony is in hard mode because the α-phase (respectively α_2-phase below the ordering temperature) has to deform in its hardest slip mode. In the soft mode, the lamellae enclose an intermediate angle (ideally 45°) with respect to the loading direction and deform easily via shear parallel to the interfacial planes. Colonies in which the lamellae are parallel to the load exhibit an intermediate yield stress [48].

The elongated shape of the β_o-grains after deformation suggests that disordered β accommodated a disproportionally large fraction of the strain (Fig. 3). This finding is in accord with literature results [49]. Additionally, it is commonly known that hot-deformation at lower temperatures leads to finer grained microstructures [50] which is confirmed by Fig. 3a and b and previous studies conducted on various TiAl alloys, e.g. Refs. [49,51,52]. Although recrystallization and recovery have long been subject of scientific research, some ambiguity concerning the classification and designation of the different annealing phenomena exists. In this work, the terminology used in references [53–55] is utilized. A detailed description of the different recrystallization and recovery mechanisms can also be found in these publications.

4.1. α-phase

The results from in-situ HEXRD experiments allow bridging the gap between the microstructural images before and after the compression experiment. In the AT-plots of both investigated

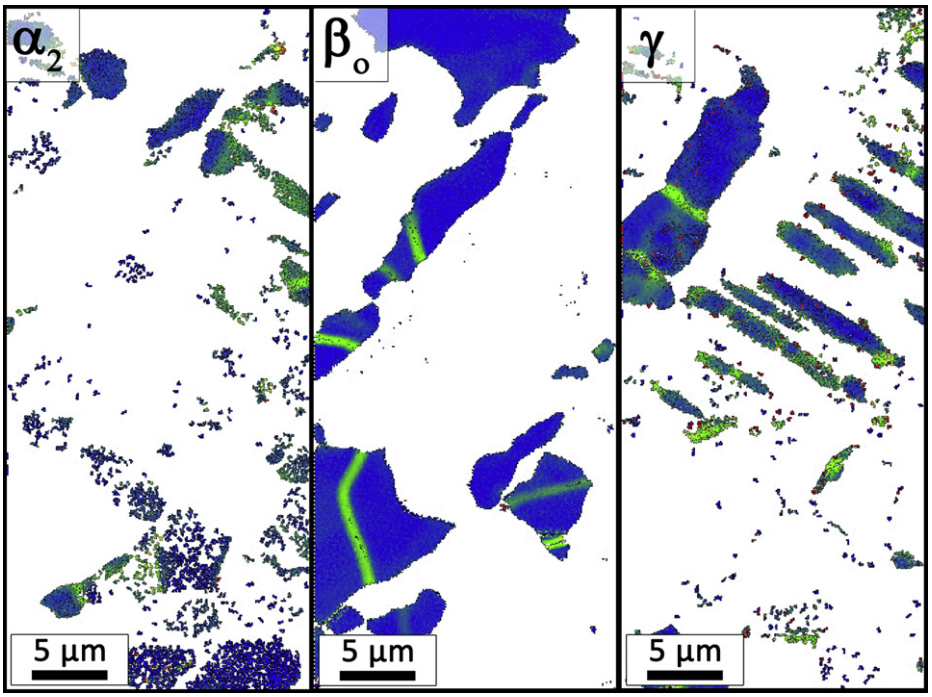

Fig. 8. Kernel average misorientation maps obtained after deformation of the specimen at 1220 °C. Due to high defect densities within the γ and the α_2-phase and the lamellar arrangement of the two phases, only the β_o-grains are imaged properly. Light colors correspond to high degrees of misorientation. Note that at 1220 °C, α and β-phase are present in their disordered states.

deformation temperatures, the α timelines tilt and broaden as soon as deformation starts (Fig. 4a and d). This indicates the occurrence of grain rotation about the beam axis and defect formation (i.e. dislocation multiplication). Timelines frequently bifurcate at 1300 °C, which is less frequently observed at 1220 °C. Bifurcation can be caused by the arrangement of dislocations into sub-grain boundaries. Consequently, it is concluded that processes which lead to sub-grain formation occur less readily at 1220 °C processes that lead to such an arrangement occur less readily. Another notable difference is that timelines remain sharper during deformation at 1300 °C, compared to deformation at 1220 °C (Fig. 4a and d).

Sharp timelines or dots appear in significant numbers at a strain of ~0.25 (at $t = 250$ s) while the material is being deformed at 1220 °C. This implies that new grains with low defect density appear after some minimum plastic strain and time. Dynamic discontinuous recrystallization (DDRX) is known to require a minimum amount of plastic deformation and a so-called incubation time [56]. Consequently, the observation of the sudden appearance of grains with low defect density can be ascribed to DDRX.

At 1300 °C, the dominant features in the AT-plot of the α 022 reflection are long timelines that show moderate broadening (Fig. 4a). Instantaneous bifurcation of timelines upon the onset of compression points toward the accommodation of defects by a continuous process that does neither require a minimum strain, nor an incubation time. An important factor in determining which process is likely to contribute most to accommodating the defects is the stacking fault energy (SFE). No accurate values of the SFE in the α/α_2-phase are to be found in literature, but there seems to be some consensus on the fact that it is high [49] which favors dynamic recovery (DRV). It should also be considered that the volume fractions of the α and β-phase at 1300 °C are significantly higher than at 1220 °C. This is important for the behavior of the α-phase because the β-phase can accommodate large strains at high temperatures (Fig. 3a). As a consequence, the α-phase is expected to experience smaller strains during deformation at 1300 °C which is also reflected by the more distinct timelines of the α phase at this temperature. Considering these facts it is concluded that the α-phase undergoes a significant degree of recovery at 1300 °C. Additionally, HAGB formation may occur by continuous recrystallization. In general, the defect densities in the α-phase are high after deformation which is in accord with the findings of Liu et al. [49].

The EBSD map of the α_2-phase after deformation at 1300 °C (Fig. 7) reveals that grains with different defect densities are present. Additionally, sub-grain boundaries are observed in the microstructure which is further evidence for the occurrence of DRV.

4.2. β-phase

Contrary to the AT-plots of the α-phase, those of the β-phase show strong similarities at the two investigated temperatures (Fig. 4b and e). In both experiments, changes in the timelines of the β-phase are obvious even before deformation starts at $t \sim 125$ s. Since no strain is imposed on the specimen at this stage, only grain coarsening and phase transformation processes can change the intensity of a diffraction spot. Strains due to different coefficients of thermal expansion can rotate crystallites by a small degree which might lead to a significant change in intensity. Although there are single timelines vanishing and appearing during this stage, continuous timelines are far more dominant. This suggests that only a few grains are affected by the aforementioned processes. As soon as the specimen is subjected to deformation, the timelines disintegrate into clouds of small, comparatively sharp reflection spots located around the position of the original timeline. Many sharp spots with low intensities within a small angular range correspond to a large number of rather small crystallites with low defect densities and small misorientations [38]. No minimum strain and no incubation time seem to be required to induce the microstructural changes reflected by the changes in the AT-plots. This behavior is characteristic for DRV which is consequently identified as the dominant process. This conclusion is supported by the fact that the bcc β-phase is presumed to have a high SFE due to its similarity to β-Ti [49,57]. Additionally, it has been found for a different TiAl alloy [49] that the β-phase accommodates a large fraction of plastic strain during hot-deformation, which is confirmed by the morphology of the β-phase shown in Fig. 3.

The main difference between the AT-plots obtained at the two different temperatures is that the reflection spots are sharper and of higher intensity at 1300 °C compared to 1220 °C (Fig. 4b and e). This behavior is attributed to the fact that thermally activated recovery processes are occurring faster at higher temperatures.

Since both experiments were performed at the same strain rate, more rapidly occurring DRV processes lead to lower defect densities in steady-state conditions. Furthermore, the flow-stress has a pronounced influence on the sub-cell size [58,59]. The lower the flow-stress, the larger the sub-cells, which explains the higher intensity of reflection spots at 1300 °C. From EBSD results (Fig. 8), it is obvious that the β_o-phase grains have low defect densities. Some sub-grain boundaries are observed, especially after deformation at 1220 °C, which could point toward DRV and DDRX. An unambiguous conclusion concerning the processes occurring in β was only possible based on the results of the in-situ diffraction experiment.

4.3. γ-phase

Deformation at 1220 °C is performed in the (α + β + γ) phase field region. During heating, the volume fraction of γ-phase is decreasing (Fig. 1b) which is reflected by the overall loss in intensity visible in the AT-plot (Fig. 5a). One important fact to notice is that the γ-phase is present in the form of globular grains in the form of lamellae within the α/γ lamellar colonies at deformation temperature. Since γ and α laths of the same colony satisfy the Blackburn orientation relationship [60], the corresponding reflections form a characteristic pattern on the Debye–Scherrer rings [61]. γ-Laths within one colony image similar to a globular γ-grain in the AT-plot. The fluctuations in intensity before deformation starts (Fig. 5a) are attributed to coarsening and phase transformation processes. As a plastic strain is imposed on the specimen, most timelines broaden and tilt. However, there are some timelines that tilt but do not broaden significantly. These timelines are believed to origin from lamellar colonies that occupy a hard orientation with respect to the compression axis. Consequently, these grains accommodate a smaller fraction of the total strain and therefore show a lower defect density than the ones occupying a soft orientation. Rotation of these grains is facilitated by the plastic deformation of grains that surround them and are deformed more readily. Coarse lamellar colonies in hard orientations are likely to persist in the deformed microstructure, since the strains imposed are too small to induce recrystallization in the γ-phase. Most lamellar colonies in soft orientation, however, recrystallize more readily because of their higher defect density. It should be noted, at this point, that the strain imposed on a lamellar colony is not only dependent on its orientation, but also on its surrounding microstructural components.

From the appearance of the AT-plot (Fig. 5) and the fact that most lamellar colonies were consumed during deformation (Fig. 3b) it is concluded, that a significant fraction of the γ-phase undergoes DDRX during hot-working at 1220 °C. Dynamic recovery occurs less readily due to the small SFE of γ (60–90 mJ/m^2 [49]). Chrapoński et al. [62] investigated a γ-TiAl based alloy which was hot-worked at 1000 °C by means of transmission electron microscopy and concluded that recrystallization as well as recovery occur

in the γ-phase which is in excellent agreement with the present study. Additionally, this publication [62] points out that there is a significant degree of deformation inhomogeneity which is also confirmed by the current results.

4.4. Flow-curve

Generally, the shape of the flow-curve can be used to determine the restoration mechanisms that are operative during hot-deformation. Flow-curves recorded during the experiment are similar to those obtained with a Gleeble thermomechanical simulator (Fig. 6). A common interpretation of flow-curves is based on their shape. Single-peak flow-curves are indicative of dynamic recrystallization, whereas a constant flow-stress is associated with the occurrence of dynamic recovery (e.g. Ref. [50]). The flow curve obtained from the experiment performed at 1300 °C exhibits an approximately constant stress level until the temperature drops (Fig. 6). This indicates that dynamic recovery processes are dominant, whereas the flow curve obtained at 1220 °C corresponds to the single-peak type indicating softening due to dynamic recrystallization. At 1300 °C, the HEXRD data show clear evidence that dynamic recovery occurs in both the α and β-phase which is in excellent accord with the observed shape of the flow-curve (Fig. 6). Deformation at 1220 °C leads to a flow curve that exhibits significant flow-softening. By HEXRD, it was found that a large fraction of the lamellar colonies decompose and that the γ-phase recrystallizes dynamically. Furthermore, α-grains were shown to recrystallize at this temperature. Since only small fractions of β are present at this temperature (see Fig. 1b), the shape of the flow curve is consistent with the findings of the HEXRD experiment.

5. Conclusion

In this paper, the hot-deformation behavior of a Ti-43.5 Al-4 Nb-1 Mo-0.1B alloy was investigated in-situ by means of high-energy X-ray diffraction. Two compression experiments were conducted at 1300 °C in the $(\alpha + \beta)$ phase field region and at 1220 °C in the $(\alpha + \beta + \gamma)$ phase field region at a mean strain rate of 0.0037 s^{-1}. It was found that the α-phase predominantly dynamically recovers at 1300 °C, whereas dynamic recrystallization is observed for strains exceeding 0.25 at 1220 °C. For the β-phase, dynamic recovery was determined as the dominant process at both temperatures. The γ-phase dynamically recovers and recrystallizes at 1220 °C. By means of in-situ high-energy X-ray diffraction, it was also possible to directly observe the behavior of lamellar colonies which initially occupied a hard orientation with respect to the compression axis. Even though some of these colonies rotated during compression, they accommodated hardly any strain. Consequently, the defect density was too low to induce dynamic recrystallization and remnant colonies were found during post-mortem microstructural examinations. Results obtained by complementary investigation methods are in good agreement with the behavior observed in the diffraction experiments. In this study, in-situ methods were used to gain insight into the microstructural evolution during hot-working of a β-containing γ-TiAl based alloy. The obtained results yield important information for future alloy design strategies and for the optimization of industrial-scale hot-deformation processes of β containing γ-TiAl alloys.

Acknowledgments

The Australian participants acknowledge travel funding provided by the International Synchrotron Access Program (ISAP) managed by the Australian Synchrotron. The ISAP is funded by a National Collaborative Research Infrastructure Strategy grant provided by the Federal Government of Australia. We also appreciate the continued support of the ESTF management. The European experimentalist wishes to express gratitude for the ESRF travel support. Specimen material was provided by GfE Metalle und Materialien GmbH Nuremberg, Germany. We are grateful to Janny Lindemann for providing flow-curves obtained in hot-compression experiments at Brandenburgische Technische Universität Cottbus.

References

[1] Kim Y-W, editor. Gamma titanium aluminides 2003. Warrendale, PA, USA: TMS; 2003.
[2] Yamaguchi M, Inui H, Ito K. Acta Mater 2000;48:307–22.
[3] Appel F, Wagner R. Mater Sci Eng R 1998;22:187–268.
[4] Kestler H, Clemens H. Production, processing and application of γ(TiAl)-based alloys. In: Leyens C, Peters M, editors. Titanium and titanium alloys. Weinheim, Germany: WILEY-VCH; 2003. p. 351.
[5] Wu X. Intermetallics 2006;14:1114–22.
[6] Cui WF, Liu CM, Bauer V, Christ H-J. Intermetallics 2007;15:675–8.
[7] Clemens H, Smarsly W. Adv Mater Res 2011;278:551–6.
[8] Lasalmonie A. Intermetallics 2006;14:1123–9.
[9] Loria EA. Intermetallics 2000;8:1339–45.
[10] Clemens H, Wallgram W, Kremmer S, Güther V, Otto A, Bartels A. Adv Eng Mater 2008;10:707–13.
[11] Clemens H, Chladil HF, Wallgram W, Zickler GA, Gerling R, Liss K-D, et al. Intermetallics 2008;16:827–33.
[12] Kremmer S, Chladil H, Clemens H, Otto A, Güther V. Near conventional forging of titanium aluminides. In: Niinomi M, editor. Ti-2007 science and technology. Sendai, Japan: The Japan Institute of Metals (JIM); 2008. p. 989–92.
[13] Wallgram W, Schmoelzer T, Cha L, Das G, Güther V, Clemens H. Int J Mater Res 2009;100:1021–30.
[14] Rizzi N. Presentation at the symposium "Structural aluminides for elevated temperature applications". New Orleans, LA, USA: TMS; 2008.
[15] Shi J-D, Pu Z, Zhong Z, Zou D. Scr Mater 1992;27:1331–6.
[16] Tetsui T, Shindo K, Kaji S, Kobayashi S, Takeyama M. Intermetallics 2005;13:971–8.
[17] Tetsui T, Shindo K, Kobayashi S, Takeyama M. Intermetallics 2003;11:299–306.
[18] Tetsui T, Shindo K, Kobayashi S, Takeyama M. Scr Mater 2002;47:399–403.
[19] Appel F, Oehring M, Paul JDH, Klinkenberg C, Carneiro T. Intermetallics 2004;12:791–802.
[20] Liu B, Liu Y, Zhang W, Huang JS. Intermetallics 2011;19:154–9.
[21] Niu HZ, Chen YY, Xiao SL, Kong FT, Zhang CJ. Intermetallics 2011;19:1767–74.
[22] Rao KP, Prasad YVRK, Suresh K. Mater Des 2011;32:4874–81.
[23] Rao KP, Prasad YVRK. Mater Sci Eng A 2010;527:6589–95.
[24] Wang G, Xu L, Tian Y, Zheng Z, Cui Y, Yang R. Mater Sci Eng A 2011;528:6754–63.
[25] Stark A, Schimansky FP, Clemens H. Solid State Phen 2010;160:301–6.
[26] Witusiewicz VT, Bondar AA, Hecht U, Rex S, Velikanova TY. J Alloys Compd 2008;465:64–77.
[27] Clemens H, Boeck B, Wallgram W, Schmoelzer T, Droessler LM, Zickler GA, et al. Experimental studies and thermodynamic simulations of phase transformations in Ti-(41-45)Al–4Nb–1Mo–0.1B alloys. In: . Mater. Res. Soc. Symp. Proc, vol. 1128. Warrendale: MRS; 2008. p. 115–20.
[28] Schmoelzer T, Liss K-D, Zickler GA, Watson IJ, Droessler LM, Wallgram W, et al. Intermetallics 2010;18:1544–52.
[29] Schloffer M, Iqbal F, Gabrisch H, Schwaighofer E, Schimansky F-P, Mayer S, et al. Intermetallics 2012;22:231–40.
[30] Liss K-D, Garbe U, Li H, Schambron T, Almer JD, Yan K. Adv Eng Mater 2009;11:637–40.
[31] Liss K-D, Yan K. Mater Sci Eng A 2010;528:11–27.
[32] Liss K-D, Schmoelzer T, Yan K, Reid M, Dippenaar R, Clemens HJ. Appl Phys 2009;106:113526.
[33] Saunders N. Phase equilibria in multi-component γ-TiAl based alloys. In: Kim YW, editor. Gamma titanium aluminides 1999. Warrendale, PA: TMS; 1999. p. 183–94.
[34] Watson IJ, Liss K-D, Clemens H, Wallgram W, Schmoelzer T, Hansen TC, et al. Adv Eng Mater 2009;11:932–7.
[35] Liss K-D, Bartels A, Schreyer A, Clemens H. Text Microstruct 2003;35:219–52.
[36] Daniels JE, Drakopoulos MJ. Sync Rad 2009;16:463–8.
[37] Lindemann J. Hot-compression tests of intermetallic TiAl alloys with the Gleeble thermomechanic simulator. Unpublished results, Cottbus; 2010.
[38] Jakobsen B, Poulsen H, Lienert U, Almer JD, Shastri SD, Sørensen HO, et al. Science 2006;312:889–92.
[39] Warren BE. X-ray diffraction. New York: Dover Publications; 1990.
[40] Margulies L, Winther G, Poulsen H. Science 2001;291:2392.
[41] Yan K, Liss K-D, Garbe U, Daniels JE, Kirstein O, Li H, et al. Adv Eng Mater 2009;11:771–3.
[42] Schmoelzer T, Liss K-D, Staron P, Mayer S, Clemens H. Adv Eng Mater 2011;13:685–99.
[43] Reimers W, Pyzalla AR, Schreyer A. Neutrons and synchrotron radiation in engineering materials science. Weinheim, Germany: WILEY-VCH; 2008.
[44] Rehrl C, Kleber S, Renk O, Pippan R. Mater Sci Eng A 2011;528:6163–72.
[45] Vorhauer A, Hebesberger T, Pippan R. Acta Mater 2003;51:677–86.

[46] Kim Y-W, editor. Structural aluminides for elevated temperature applications. Warrendale, PA, USA: TMS (The Minerals, Metals & Materials Society); 2008.
[47] Kim Y-W. Acta Mater 1992;40:1121–34.
[48] Inui H, Kishida K, Misaki M, Kobayashi M, Shirai Y, Yamaguchi M. Phil Mag A 1995;72:1609–31.
[49] Liu B, Liu Y, Li YP, Zhang W, Chiba A. Intermetallics 2011;19:1184–90.
[50] Dieter GE. Mechanical metallurgy. Boston: McGraw Hill Higher Education; 1989.
[51] Appel F, Kestler H, Clemens H. Forming. In: Westbrook JH, Fleischer RL, editors. Intermetallic compounds – principles and practice: progress. Chichester, UK: John Wiley & Sons Ltd.; 2002. p. 617–42.
[52] Seetharaman V, Semiatin SL. Met Mat Trans A 1996;27:1987–2004.
[53] Kassner M, Barrabes S. Mater Sci Eng A 2005;410–411:152–5.
[54] Doherty R, Hughes D, Humphreys F, Jonas J, Jensen DJ, Kassner M, et al. Mater Sci Eng A 1997;238:219–74.
[55] Gourdet S, Montheillet F. Mater Sci Eng A 2000;283:274–88.
[56] Humphreys FJ, Hatherly M. Recrystallization and related annealing phenomena. Pergamon Press Ltd; 2004.
[57] Leyens C, Peters M, editors. Titanium and titanium alloys. Weinheim, Germany: Wiley-VCH; 2003.
[58] Raj S, Pharr GM. Mater Sci Eng 1986;81:217–37.
[59] Orlová A. Mater Sci Eng A 1996;220:281–5.
[60] Blackburn MJ. Jaffee RI, Promisel NE, editors. The science, technology and application of titanium. Oxford: Pergamon Press Ltd; 1970. p. 663.
[61] Liss K-D, Bartels A, Clemens H, Bystrzanowski S, Stark A, Buslaps T, et al. Acta Mater 2006;54:3721–35.
[62] Chrapoński J, Rodak KJ. Microscopy 2006;223:298–301.